Freestanding 3D nanoporous Cu@1D Cu_2O nanowire heterostructure: From facile one-step protocol to robust application in Li storage

Wenbo Liu,[a,d,*] Long Chen,[a] Liu Cui,[b,d] Jiazhen Yan,[a] Shichao Zhang,[c] Sanqiang Shi[d]

[a] School of Manufacturing Science and Engineering, Sichuan University, Chengdu 610065, China

[b] Key Laboratory of Condition Monitoring and Control for Power Plant Equipment, Ministry of Education, North China Electric Power University, Beijing 102206, China

[c] School of Materials Science and Engineering, Beihang University, Beijing 100191, China

[d] Department of Mechanical Engineering, The Hong Kong Polytechnic University, Hung Hom, Kowloon, Hong Kong

Tel: +86-028-85405320; Fax: +86-028-85403408; E-mail: liuwenbo_8338@163.com.

† Electronic supplementary information (ESI) available. See DOI:

Structural deterioration and low conductivity are key factors to give rise to severe capacity fading of transition metal oxides as anode for lithium-ion batteries (LIBs). An effective way to overcome this challenge is to construct nanosized metal oxide heterostructures integrated with 3D nanoarchitectured metal matrix to buffer volume variation, reinforce structural stability and improve electronic conductivity. Herein, a facile and effecitve underpotential oxidation (UPO) assisted dealloying protocol has been developed successfully to synthesize freestanding monolithic 3D nanoporous copper@1D cuprous oxide nanowire networks (3D NPC@1D Cu_2O NWNs) heterostructures. Based on their dealloying behavior, the evolution law can be well-established, sequentially described as "dealloying of (Mn, Cu) accompanying Cu_2O NWs germination", "growth of Cu_2O NWs accompanying (Mn, Cu) re-dealloying" and "Cu_2O NWNs coarsening". Compared to other Cu_xO-based electrode materials with different structure designs reported in the literature, the unique nanocomposites as anode for LIBs exhibit extremely superior Li storage performance including ultrahigh initial reversible capacity of 2.71 mAh cm^{-2}, good cycling stability with 60.2% capacity retention after 150 cycles (just 0.007 mAh cm^{-2} per cycle for capacity fading), and excellent rate capability with reversible capacity as high as 1.64 mAh cm^{-2} after 55 high-rate cycles. This mainly originates from effectively accommodating huge volume changes during charge/discharge processes, providing abundant reaction active sites, shortening electron/ion transport paths, and building reliable 3D/1D composite nano-configuration without additional binders and conductive agents, indicative of a considerably promising anode candidate toward

high-performance LIBs.

Keywords: Dealloying; One-step protocol; Cu@Cu_2O heterostructure; 1D Nanowire; Lithium ion battery

Introduction

Nowadays, transition metal oxides have aroused great interest for various applications including field effect transistors,[1,2] solar cells,[3,4] gas sensors,[5-7] and catalyst supports,[8,9] and so forth. Owing to their unusual multiple oxidation states, the outstanding electrochemical performance toward redox reactions can be achieved easily.[10-16] Particularly, in recent years, they have been proposed as promising anode materials for LIBs due to significantly higher theoretical capacities than conventional graphite anodes (just 372 mAh g^{-1}) on a basis of incorporation of more than one Li with them. Typically, Tarascon et al.[17] have demonstrated that electrodes made of transition metal oxides exhibit extremely superb electrochemical properties. Among them, copper(I/II) oxide would be especially appealing in LIBs because of their good performance, low cost, natural abundance and environmental friendliness. Despite of these advantages, they also suffer from drastic volume changes and poor electronic conductivity during lithiation/delithiation processes, leading to fierce capacity decay.

To solve these issues, copper oxide nanoparticles with different morphologies and valence/electronic states of copper have been developed and studied widely, such as CuO nanohexagons,[18] CuO hollow nanospheres,[19] Cu_2O nanospheres,[20] and Cu_2O nanocubes.[21] Although nanoparticles could reduce the diffusion length for Li^+ transports and accommodate the mechanical strain during Li insertion/extraction, they still have obvious drawbacks like poor thermodynamic stability and marked aggregation effect due to large surface area and high surface energy.[22,23] Thus, there could be much room for progress with regard to the development of copper oxide

nanostructures, especially in structure design, morphology control and size uniformity, which needs to be investigated deeply.

1D nanostructure is of considerable potential as key functional components for LIBs due to their unique and fascinating properties resulting from distinct migration path and quantum confinement effect,[24-26] while 3D nanoporous architecture as superior anode supports can provide efficient and rapid pathways for Li^+/electron transports and short solid-state diffusion lengths.[27-29] Rational combination of 1D nanosized metal oxide and 3D nanoporous metal matrix could generate a huge amount of heterojunctions to gain the novel functions and enhanced properties which cannot be realized simply from each of the components separately.[30-33] In particular, the heterojunctions as anode for LIBs could possess main advantages as follows: (1) 1D nanowires (NWs) with large specific areas provide abundant active sites for lithiation reactions and short path lengths for Li^+/electron transports to facilitate high capacity and rate performance;[34] (2) Huge volume change induced by lithiation/delithiation processes can be accommodated and buffered by adequate room amongst 3D/1D composite nanoarchitecture;[35] (3) Homogeneous dispersion of 1D NWs on 3D nanoporous matrix prevents aggregation of NWs and enhances conductivity due to partition effect of nanopores and low charge transfer resistance.

Herein, we developed a facile and effective UPO assisted dealloying protocol to synthesize freestanding monolithic 3D NPC@1D Cu_2O NWNs by one-step electrochemical dealloying of as-cast Mn 35 at.% Cu alloy sheets in an oxygen-containing H_2SO_4 solution at the potential of -0.2 V(SCE), which is 123

mV(SCE) lower than the critical oxidation potential of metal Cu in the H_2SO_4 solution. The 1D Cu_2O NWNs growing on 3D NPC matrix in situ can maintain high conductivity and effectively avoid the use of binders and conductive agents, which is currently indispensable in commercial LIBs but inevitably cause a depressed energy density. Compared to other Cu_xO-based electrode materials with different structure designs reported in the literature, the created nanocomposites by the one-step strategy exhibit the extremely superior Li storage performance including the extraordinarily high specific capacity, good cyclability and excellent rate capability, indicative of a considerably promising candicate for high-performance LIB anodes. The formation mechanism of the unique 3D NPC@1D Cu_2O NWNs and their robust application in LIBs have been discussed systematically.

Experimental

Mn-Cu alloy with nominal composition of 35 at.% Cu was prepared from pure Mn (99.99 wt.%) and pure Cu (99.999 wt.%). Voltaic arc heating was employed to melt the powder in a copper crucible under an argon atmosphere, and then the melt was cooled down into ingots. The Mn 35 at.% Cu ingots subsequently were processed into sheets with thickness of ca. 200 μm by low speed wire-cutting electrical discharge machine. Prior to further treatment, the alloy sheets were degreased with acetone, and then ground and mechanically polished with sand papers and alumina slurry in turn to eliminate oxides formed on the surface during processing and make it become a mirror-like plane. EDX analysis showed the atomic percentage of Cu and Mn in the initial Mn-Cu alloy was quite closely to the designed composition, indicating the alloy

sheets can be further used in the following study (Table S1, ESI†). Then, the Mn 35 at.% Cu alloy sheets were electrochemically dealloyed in a 5 wt.% H_2SO_4 aqueous solution without removal of oxygen (called oxygen-containing H_2SO_4 solution in this work) at RT (ca. 25℃) at the potential of -0.2 V(SCE) for different durations to obtain the ideal freestanding 3D NPC@1D Cu_2O NWNs. After the dealloying, the specimens were rinsed with distilled water and dehydrated alcohol (analytical grade) several times, then dried at 70℃ for 24 h in vacuum, and eventually kept in a vacuum chamber to avoid oxidation further.

Microstructural characterization and analysis of the initial Mn 35 at.% Cu alloy and as-dealloyed nanocomposites were made using X-ray diffraction (XRD, Rigaku D/Max-2400) with Cu K_α radiation (λ=1.5406 Å), scanning electron microscopy (FESEM, Hitachi S-4800) with an EDX analyzer, transmission electron microscopy (TEM, JEOL JEM 2100F) with selected-area electron diffraction (SAED), and high-resolution transmission electron microscopy (HRTEM, JEOL JEM 2100F).

Potentiodynamic polarization, potentiostatic polarization and cyclic voltammetry (CV) were performed using an electrochemical workstation (PARSTAT 2273) in a standard three-electrode cell (200 mL) with a Pt plate electrode as a counter electrode, a saturated calomel electrode (SCE) as a reference electrode, and a tested metal/alloy (including the as-cast Mn-Cu alloy, metals Mn and Cu for comparison) as the working electrode. All measurements were carried out in solutions exposed to air at RT. The electrolyte was a 5 wt.% oxygen-containing H_2SO_4 solution using analytical-grade reagents and distilled water. The scan rates were 5 mV/s for potentiodynamic

polarization and 1 mV/s for CV measurements, after allowing a steady state potential to develop. A total of 500 cycles of CVs were recorded for the as-cast Mn-Cu alloy. The applied potential for electrochemical dealloying of the as-cast Mn-Cu alloy was determined according to potentiodynamic polarization test results. The amperometric i-t curves were obtained during potentiostatic polarization.

Electrochemical charge-discharge behaviors were investigated in simulant cells assembled with the as-prepared composite anode, lithium foil and Celgard 2300 membrane in an Ar-filled glove box (MB-10-G with TP170b/mono, MBRAUN). Electrolyte was 1M $LiPF_6$ in a mixed solution of EC, DEC and DMC (1:1:1 by v/v/v). Each cell was aged for 24 h at RT before commencing the electrochemical tests. The galvanostatic charge-discharge measurements were carried out in a multichannel battery test system (NEWARE BTS-610, Newware Technology Co., Ltd., China) for a cut-off potential of 0.01-3.0 V (vs. Li/Li^+) at ambient temperature. The delithiated electrode after repeated cyclings was taken out of the cell, washed with ethanol to remove the residual electrolyte and lithium salts and then dried at RT for further SEM characterization. Cyclic voltammograms (CVs) were recorded between 0.01 and 3.0 V (vs. Li/Li^+) at a scan rate of 0.1 mV s^{-1}. Electrochemical impedance spectroscopy (EIS) measurements were performed in the frequency range of 10 mHz-100 kHz with an AC voltage amplitude of 5 mV. Both CVs and EIS were carried out using a PARSTAT 2273 electrochemical workstation.

Results and discussion

The as-cast Mn 35 at.% Cu alloy sheets and as-produced nanocomposites upon the

dealloying in the H_2SO_4 solution at -0.2 V(SCE) for 60 min are characterized by XRD, with typical patterns shown in Figure S1 (ESI†). The filled circle, square, and triangle stand for (Mn, Cu), Cu and Cu_2O, respectively. The Mn 35 at.% Cu alloy is composed of single-phase (Mn, Cu) solid solution (Figure S1a, ESI†). Upon the dealloying, three major diffraction peaks (2θ=43.3, 50.4 and 74.1°) can be found clearly in the XRD pattern, assigning to the (111), (200) and (220) reflections of face centered cubic (f.c.c.) Cu, respectively. Meanwhile, there also exist two minor diffraction peaks (2θ=36.5 and 41.6°) corresponding to the (111) reflection of emerged Cu_2O and the (111) reflection of residual (Mn, Cu), respectively. Note that other diffraction peaks of Cu_2O, such as those at 42.4°, 61.5° and 72.7°, cannot be discerned readily due to its low content and partial overlaps with $(111)_{Cu}$ and $(220)_{Cu}$ reflections. As a result, the as-obtained nanocomposites are mainly composed of Cu and Cu_2O phases aside from a little residual (Mn, Cu) precursor, in which Cu is dominant obviously in terms of its high peak intensity (Figure S1b, ESI†). Figure 1a schematically illustrates the electrochemical preparation process of the nanocomposites through one-step UPO assisted dealloying protocol and Figure 1b-h shows their typical plane and cross-sectional microstructures. As can be seen from Figure 1b, the specimen surface exhibits a uniform porous network with 3D nanoarchitecture consisting of 1D NWs. The SEM image at a higher magnification further shows the length scale of single NW is hundreds of nm but its diameter only ranges from several to a dozen nm (Figure 1c). Intriguingly, the section view of the nanocomposites displays that these 1D NWs can be anchored well on nanoporous matrix with unimodial pore size

distribution and a typical SEM image is presented in Figure 1d. The high-magnification SEM image further exhibits an open, bicontinuous interpenetrating ligament-pore structure, suggesting that the nanoporous substrate is 3D (Figure 1e). Moreover, the TEM observations also reveal that the superficial 3D porous network configuration is composed of 1D NWs with 15±5 nm in diameter and a typical single NW is shown in the inset of Figure 1f. The SAED pattern corresponding to the single NW shows a typical hexagonal pattern, which is from the cubic Cu_2O [110] zone axis, indicating a single crystalline characteristic of the selected target (Figure 1g). Meanwhile, the lattice fringes with interplanar spacing of 0.245 nm extending throughout the whole NW from the HRTEM image in Figure 1h further verify the single crystal nature of 1D Cu_2O NW. In addition, EDX analysis shows both Cu and O can be identified from the surface of nanocomposites (Figure 1i), while nearly just Cu can be detected from the cross-sectional nanoporous matrix (Figure 1j), confirming that the 1D NWs on the surface are Cu_2O and the nanoporous structure underneath is Cu in combination with the XRD analysis above. Note that the existence of a trace amount of Mn mainly derives from the residual undealloyed (Mn, Cu) precursor, which could be expected to be trapped inside Cu ligaments based upon the established dealloying physical mechanism of solid solution alloys.[36,37] Thus, the as-synthesized nanocomposites possess unique freestanding monolithic 3D nanoporous copper supported 1D cuprous oxide nanowire network heterostructures. In stark contrast, no obvious 1D NWs can be observed on the surface of products by chemcial dealloying of the as-cast Mn 35 at.% Cu alloy under the same conditions

(Figure S2, ESI†), clearly demonstrating that the present one-step electrochemcial synthesis protocol developed has an exclusive virtue on constructing reliable 3D/1D composite nano-configuration without additional binders and conductive agents that are currently indispensable in commercial LIBs but inevitably give rise to a markedly reduced energy density.

To reveal the formation mechanism, surface morphology and chemical composition evolutions of the freestanding 3D NPC@1D Cu_2O NWNs nanocomposites during the dealloying were investigated systematically. Figure 2a-d displays the morphology evolution of 1D Cu_2O NWNs on the surface of 3D NPC matrix during the dealloying. Clearly, with the increase of dealloying duration from 10 to 60 min, smallish grass-like Cu_2O NWs can be emerged uniformly on the surface of matrix firstly and then continuously grows up along the radial and axial directions but their aspect ratio increases sharply, eventually resulting in the in-situ formation of 3D NPC@1D Cu_2O NWNs (Figure 2a-c). Subsequently, the 1D NWNs start to agglomerate regionally and coarsen gradually to create some uneven backbones as the dealloying duration reaches as long as 80 min (Figure 2d). Figure 2e shows the composition variation of the Mn 35 at.% Cu alloy with dealloying duration as measured by EDX. Obviously, three composition regions, denoted by I, II and III, can be distinguished. It can be seen clearly from region I that the atomic percentages of both Mn and Cu alter dramatically, while those counterparts in region II spanning dealloying duration from 10 to 60 min only vary mildly; thereafter, a slighter composition change can be observed in region III. Note that the composition changes little, close to a steady state, as the dealloying

duration up to 80 min.

To address this issue in the spirit of exploration, we consider that their formation mechanism could be explained as follows based on a combination of morphology and composition evolutions of the unique nanocomposites, as schematically illustrated in Figure 2f. Before dealloying, the initial Mn 35 at.% Cu alloy is composed of single (Mn, Cu) solid solution. With increasing dealloying duration, the dealloying process can be divided into three stages, signified by stage I, stage II and stage III, respectively. In stage I, the component Mn in the Mn-Cu alloy acting as an anode dissolves preferentially. Typically, the Mn in (Mn, Cu) continuously dissolves into the solution and the remaining Cu atoms will reassemble to form the nanoporous structure through rapid surface diffusion along the alloy/solution interfaces; meanwhile, the dissolved active oxygen radical (•O) in the corrosive solution can be captured fast by activated Cu atoms on the surface with unsaturated bond and high surface energy to create the smallish grass-like Cu_2O NWs under the action of external electric field, which is in good line with the SEM observations described above. This process could correspond to the dramatic alterations of atomic percentages of both Mn and Cu, as well as the moderate increase of that of O in region I of Figure 2e due to the dissolution of a large amount of Mn and the generation of a small quantity of Cu_2O. Hence, stage I can be indentified as “dealloying of (Mn, Cu) accompanying Cu_2O NWs germination”, corresponding to the initial stage of dealloying. In stage II, the 1D Cu_2O NWs grow continually coupled with the further evolution of nanoporous architecture deriving from the gradual exposure and redissolution of Mn in the

undealloyed (Mn, Cu) embedded in the Cu ligaments through diffusion and rearrangement of Cu atoms. At this stage, the solution hardly can contact the undealloyed (Mn, Cu) directly but always can contact the Cu_2O NWs readily, and as a result, the atomic percentages of both Mn and Cu only vary mildly while the counterpart of O increases markedly, suggesting that the growth of 1D Cu_2O NWs is predominant relative to nanoporous structure evolution at this moment. The end of this stage is marked by the occurrence of regional agglomeration of 1D Cu_2O NWs. It could be defined as "growth of Cu_2O NWs accompanying (Mn, Cu) re-dealloying" stage, corresponding to the composition evolution process in region II of Figure 2e spanning dealloying duration from 10 to 60 min. In stage III, the uniform 1D Cu_2O NWs begin to agglomerate and coarsen locally due to the occurrence of Ostwald ripening from the high mobility of Cu atoms in the acidic solution for a relatively long duration, corresponding to the slight changes in chemical compositions of all components as the dealloying duration exceeds 60 min. It should be noted that the atomic percentages of both Mn and Cu decrease very slowly, accompanied by a corresponding rise in the O concentration, and eventually, a quasi-stable state can be achieved with the dealloying duration up to 80 min. This present result suggests that the regional coarsening of 1D Cu_2O NWNs is prominent at this stage, which could be designated as "Cu_2O NWNs coarsening". This mechanism may lead to the case that the dealloying of (Mn, Cu) solid solution and the in-situ growth of Cu_2O NWNs can be achieved simultaneously during the one-step electrochemical dealloying and holds accountable for the in-situ formation of freestanding 3D NPC@1D Cu_2O NWNs.

Figure 3a shows Tafel polarization curves of metals Mn, Cu and as-cast Mn 35 at.% Cu alloy in the H_2SO_4 solution at RT, respectively. It can be found that the critical corrosion potential (E_{corr}) of the Mn-Cu alloy is -0.621 V(SCE), which is much greater than that of metal Mn (-1.299 V(SCE)) but far lower than that of metal Cu (-0.077 V(SCE)), indicating that a relatively large difference exists in the metal/metal-ion equilibrium potentials between Mn and Cu, and element Mn is more electroactive. For the initial Mn 35 at.% Cu alloy comprising single-phase (Mn, Cu) solid solution, components Mn and Cu existing in the alloy can form highly effective galvanic cell, in which the Mn acts as an anode to preferentially dissolve accompanying diffusion and rearrangement of Cu atoms along the alloy/solution interfaces to eventually form the 3D NPC matrix with unimodal pore size distribution. Moreover, it is worthwhile noting that the applied potential for electrochemcial dealloying of the as-cast Mn-Cu alloy is -0.2 V(SCE), 123 mV(SCE) lower than the E_{corr} value of metal Cu but at which Cu_2O NWs can be generated, indicative of the occurrence of oxidation of Cu to Cu_2O beneath the critical potential during the electrochemical dealloying. Thus, we herein define this abnormal electrochemical oxidation process as underpotential oxidation (UPO) and name this unique dealloying technique as UPO assisted dealloying. Figure 3b displays the current density *versus* duration profile of the as-cast Mn 35 at.% Cu alloy dealloyed in the H_2SO_4 solution at the potential of -0.2 V(SCE). Clearly, with the dealloying duration increasing to 80 min, the corrosion current density declines continuously and presents a distinctly fast-slow-fast-slow four-step tendency. This result can further confirm, from an

electrochemical perspective, that the dealloying of the as-cast Mn-Cu alloy includes the Mn dissolution from (Mn, Cu) solid solution, the Cu_2O generation, growth and coarsening. Note that as the dealloying duration is less than 30 min, the regular zigzag variation trend of current density can be observed in the magnified inset of Figure 3b, which is closely related to the typical dynamic competition between dissolution of Mn atoms and diffusion-rearrangement of Cu atoms during dealloying.[38] Figure 3c presents the corrosion duration dependence curve of open circuit potential (E_{open}) during the electrochemical dealloying; as a reference, the counterpart during the chemical dealloying under the same conditions also was added. Analogously, the E_{open} variation also exhibits fast-slow-fast-slow four stages in the whole test range, well consistent with the change tendency of corrosion current density in Figure 3b. It should be noted that the E_{open} during the electrochemical dealloying is always higher than that during the chemical dealloying at any same duration, implying that the content of Cu in the as-dealloyed specimens could be always higher after the electrochemical dealloying for same duration, which can be rationally explained as a consequence of accelerated dissolution of Mn by external electric field as additional driving force. Figure 3d displays the CVs of the as-cast Mn 35 at.% Cu alloy in the H_2SO_4 solution in the voltage window of -0.65 ~ -0.3 V(SCE) at a scan rate of 1 mV s^{-1}, in which -0.65 V(SCE) is lower than E_{corr} of (Mn, Cu) solid solution and -0.3 V(SCE) is higher than that but lower than E_{corr} of metal Cu. Also shown are the CVs of metals Mn and Cu for comparison in Figure 3e-f. Clearly, the CVs of metal Mn has a sharp increase of current density during the forward and reverse scans, while the

current density of metal Cu has no obvious change in the whole voltage window. For the CVs of the Mn 35 at.% Cu alloy up to 500 cycles, there is a distinct shift from oblique to horizontal direction with increasing cycle number, indicating that the CVs of the Mn-Cu alloy evolve gradually from the Mn-type to the Cu-type as the dealloying happens continuously. Therefore, the one-step UPO assisted dealloying technique developed in this work provides a brand-new and high-efficient approach to in-situ construct 3D nanostructured metal/oxide composites with broad application prospects in various industries.

The Li storage performance of the unique 3D NPC@1D Cu_2O NWNs as anode for LIBs is discussed systematically in the following section. For a rational comparison, the 2D PC@Cu_2O MPs electrode (Figure S3, ESI†) is also introduced in some tests to verify the superiority of the 3D electrode, which can be obtained typically by two-step heat treatments of 2D PC at 550℃ for 1 h under ambient atmosphere following at 700℃ for 2 h under Ar atmosphere. Figure 4a and b shows the galvanostatic charge-discharge curves of 3D NPC@1D Cu_2O NWNs and 2D PC@Cu_2O MPs electrodes between 0.01 and 3.0 V (vs. Li/Li^+) at the constant current density of 0.1 mA cm^{-1}, respectively. For the 3D NPC@1D Cu_2O NWNs electrode, two obvious discharge plateaus can be observed at 1.7-1.2 V (vs. Li/Li^+) and 1.2-0.4 V (vs. Li/Li^+) in the first discharge process, which corresponds to the lithiation of Cu_2O ($Cu_2O + 2\ Li^+ + 2\ e^- \rightarrow Li_2O + 2\ Cu$) and the formation of solid electrolyte interphase (SEI) membrane.[39,40] Noted that the two plateaus shorten during the subsequent discharge processes compared to the first one, which can be ascribed to the activation of

electrode fully permeated by electrolyte just after the initial discharge process.[41] Moreover, a relatively large capacity loss can be found between the first and second discharge processes, which is mainly related to the formation of SEI causing the irreversible electrolyte decomposition.[42,43] Analogously, there also exists two plateaus of 1.1-2.1 V (vs. Li/Li^+) and 2.3-2.8 V (vs. Li/Li^+) in the initial charge processes, assigned to the decomposition of SEI and the occurrence of delithiation reaction ($Li_2O + 2\ Cu \rightarrow Cu_2O + 2\ Li^+ + 2\ e^-$), respectively. Except for the initial discharge, the shapes of the charge and discharge curves do not change remarkably afterwards, implying its good capacity retention. This is mainly owing to the plenty of interspace among 1D Cu_2O NWNs alleviating the large volume change during charge-discharge processes and the in-situ growth of 1D Cu_2O NWNs on 3D NPC matrix suppressing the structure collapse, pulverization and exfoliation happening in active components. Additionally, it is worthwhile noting that the voltage plateau ranges of charge and discharge curves vary little in the first 10 cycles, suggesting the superior structure integrity and cycling stability of 3D NPC@1D Cu_2O NWNs electrode.

In contrast, for the 2D PC@Cu_2O MPs electrode, just single sloping potential range of 1.3-0.5 V (vs. Li/Li^+) can be found in the initial discharge process, which involves both the reduction of Cu_2O and the formation of SEI.[44,45] It has been reported that the plateau overlap is likely related to the large Cu_2O sizes with typical micron-scale, which can decrease the lithiation potential of Cu_2O markedly.[44] This is in good line with the SEM observations presented in Figure S3 (ESI†). Intriguingly, like the 3D structured electrode, the two discharge plateaus of 1.5-1.1 V (vs. Li/Li^+) and 0.75-0.3

V (vs. Li/Li^+) emerged in the second discharge process, indicating the Cu_2O lithiation and SEI formation happening at the exactly different potential ranges, which can be attributed to the typical scale change of Cu_2O from micron to nanometer during the initial charge-discharge process, resulting in the lithiation potential shift of Cu_2O to the higher one.[44,45] Similarly, the initial charge process only has one sloping potential range from 0.7 to 2.5 V (vs. Li/Li^+), corresponding to the decomposition of SEI and the oxidation of Cu to Cu_2O.[45] It should be noted that all the charge curves of 2D PC@Cu_2O MPs electrode show a quite steep change tendency, implying the greater difficulty in delithiation process of micron-sized Cu_2O with less specific areas and active sites than those in nanoscale. After the 3rd charge-discharge cycle, no distinct lithiation and delithiation plateaus still can be observed clearly, accompanied by the fast decay of capacity. The charge capacity remains as low as 0.3 mAh cm^{-2} at the 10th cycle, just with capacity retention of 35.1%. This is mainly associated with the huge volume variation inducing the cracking, pulverization and detachment of active material from current collector during repeated cyclings.

To investigate the electrochemical mechanism during charge-discharge processes, the first three-cycle CVs of 3D NPC@1D Cu_2O NWNs electrode were measured with a potential range of 0.01-3.0 V (vs. Li/Li^+) at a scan rate of 0.1 mV s^{-1}. As shown in Figure 4c, two broad cathodic peaks can be observed clearly around 1.38 and 0.61 V (vs. Li/Li^+), which can be assigned to the reversible conversion of Cu_2O to Cu, as well as the formation of SEI. During the first charge process, the two anodic peaks emerging at 1.67 and 2.72 V (vs. Li/Li^+) correspond to the decomposition of SEI and

oxidation of Cu to Cu_2O. Note that the peak intensity of SEI formation is relatively larger than that of the decomposition, indicative of the incomplete reaction process. The redox peak positions during the subsequent cycles have little deviation from those of the initial cycle, demonstrating its excellent structure stability and electrochemical reversibility, which is in good accordance with the galvanostatic charge-discharge results present in Figure 4a.

On the contrary, the initial-cycle CVs of 2D PC@Cu_2O MPs electrode differed significantly from the following cycles, as shown in Figure 4d. Clearly, in the 1st scan, just single reduction peak can be observed and then splitted into two peaks in the subsequent cathodic scans. It should be noted, however, that two reduction peaks can be obtained directly in the initial cycle of the 3D structured electrode with typical feature size in nanoscale, which can effectively raise the Cu_2O lithiation potential as well as enlarge the potential difference between Cu_2O lithiation and SEI formation in comparison with conventional micron-sized one.[27,46] Additionally, the individual peak intensity and area integral of 2D PC@Cu_2O MPs electrode are reduced markedly with increasing cycle number, suggesting that the initial capacity is lost rapidly in a continuous way during the first three cycles. This is correlated to its typical size and structure change during cyclings, resulting in the poor structure integrity and stability. Thus, the uniuqe 1D nanostructure design in the 3D electrode is more beneficial to maintain the structure integrity and stability of Cu_2O during cyclings relative to the large-sized microparticles in the 2D electrode.

Cycling stability is a key indicator to evaluate the superiority of electrode. Figure

4e illustrates the cycle performance of 3D NPC@1D Cu_2O NWNs electrode with a potential range of 0.01-3.0 V (vs. Li/Li^+) at a current density of 0.1 mA cm^{-2}; meanwhile, the counterpart of 2D PC@Cu_2O MPs electrode also is added as a comparison. It is clear that the 3D NPC@1D Cu_2O NWNs electrode delivered the large discharge and charge specific capacities of 4.35 mAh cm^{-2} and 2.71 mAh cm^{-2} in the initial cycle, respectively, with a relatively high first coulombic efficiency beyond 62.2%. The reversible capacity retention of the 3D electrode reaches as high as 78.9% after first 10 cycles and still can retain beyond 60.2% after 150 cycles, which means just 0.007 mAh cm^{-2} per cycle for capacity fading. Note that except for the first several cycles, its coulombic efficiency always maintains above 95% and no obvious capacity decay occurs in the subsequent elongated cycles, indicative of the superior electrochemical reversibility. Typically, the reversible capacities of 1.96, 1.77 and 1.67 mAh cm^{-2} can be achieved at the 20th, 50th and 120th cycles for the 3D electrode, respectively. Even after 150 cycles, it still can deliver a high reversible capacity of 1.63 mAh cm^{-2}. The outstanding electrochemical property can be ascribed to the reliable 3D/1D composite nano-configuration design accommodating the huge volume variation and enhancing the loadings of active material. In contrast, the initial discharge and charge capacities of 2D PC@Cu_2O MPs electrode are only 2.24 mAh cm^{-2} and 1.15 mAh cm^{-2}, respectively, with a relatively low coulombic efficiency of 51.3%. In the subsequent cycles, the reversible capacities of 0.26, 0.15 and 0.076 mAh cm^{-2} can be attained for the 2D electrode at the 20th, 50th, 150th cycles, respectively. Obviously, the areal capacity of 2D PC@Cu_2O MPs electrode sharply

decreases from the beginning and only 6.6% capacity retention remains after 150 cycles with coulombic efficiency below 85%. This can be main relation to the close stacking of Cu_2O particles and their relatively large feature sizes, which would lead to the rapid cracking, pulverization and detachment of Cu_2O from 2D PC substrate induced by the huge volume change and insufficient stress buffering during the lithiation/delithiation processes. In addition, we give a detailed comparison of lithium storage properties of the 3D NPC@1D Cu_2O NWNs electrode with other Cu_xO-based electrode materials reported in the recent literature, as listed clearly in Table S2 (ESI†). Obviously, the as-built 3D electrode by one-step dealloying route possesses the significantly improved cycling ability with higher specific capacity, longer cycle life and more steady coulombic efficiency.

Rate performance is another important consideration. Rate capability profiles of 3D NPC@1D Cu_2O NWNs and 2D PC@Cu_2O MPs electrodes at the different current densities were further measured, as displayed in Figure 4f. Clearly, the 3D electrode can deliver the high reversible capacities of 1.12, 0.51 and 0.35 mAh cm^{-2} at the current densities of 0.2, 0.4 and 0.8 mA cm^{-2}, respectively. When the current density returned back to 0.1 mA cm^{-2} at the 45th cycle, the reversible capacity increases to 1.73 mAh cm^{-2}, which reserves as high as 93.7% capacity retention compared with the 11th cycle at the same current density. It is worth noting that after undergoing a series of high-rate charge-discharge processes, the reversible capacity still can maintain 1.64 mAh cm^{-2} at the 55th cycle, fully demonstrating its excellence for rate performance. This outcome can be attributed to the unique 1D NWNs structure with large specific

area and enough interspace, which can not only endow the better electrolyte infiltration, but also provide the larger contact areas and more active sites for lithiation/delithiation reactions. Meanwhile, the in-situ growth of Cu_2O NWNs on 3D NPC matrix (without additional binders and conductive agents) also can reinforce the binding force effectively between active material and current collector, withstand the pulverization and detachment of active material from current collector caused by the volume change, and shorten the Li^+/electron diffusion paths during charge-discharge processes. In contrast, the 2D PC@Cu_2O MPs electrode just can deliver the reversible capacities of 0.10, 0.03 and 0.01 mAh cm^{-2} at the current densities of 0.2, 0.4 and 0.8 mA cm^{-2}, respectively. When the current density was reduced to 0.1 mA cm^{-2} again, the reversible capacity cannot pick up a higher value (namely failure in essence), indicative of its extremely poor rate capability. This is primarily because the repeated huge volume expansion and contraction of Cu_2O MPs at the high current density is much easier to bring about the rapid cracking, pulverization and exfoliation of active material as well as the collapse and severe damage of electrode configuration.

Figure 4g-h further exhibits the charge and discharge cruves of 3D NPC@1D Cu_2O NWNs electrode at various current densities from 0.1 to 1.6 mA cm^{-2}. Obviously, the initial discharge and charge capacity retention is gradually reduced to 83.9%, 69.9% and 94.8%, 82.3% at the current densities of 0.2 and 0.4 mA cm^{-2}, respectively. Even as the current density reaches 1.6 mA cm^{-2}, the initial discharge and charge capacity retention still retains as high as 54.1% and 69.4%, confirming its excellent kinetics characteristics. Moreover, with the increase of current densities, both the discharge

potential decrease and charge potential increase are not obvious, suggesting a little polarization of electrode. It can be probably related to the unique 3D/1D composite nano-configuration and the in-situ growth of single-crystal Cu_2O on NPC substrate, which can not only provide the favorable conductive environment for active material, but also decrease the charge transfer resistance effectively between active material and current collector. This will be discussed in detail in the following part.

The ion and electron transports of 3D NPC@1D Cu_2O NWNs and 2D PC@Cu_2O MPs electrodes were investigated by EIS, as depicted in Figure 4i and j, which is one of the most important ways to reveal the Li^+ and electron transport kinetics in LIBs. As indicated in Figure 4i, both Nyquist plots consist of a semicircle in high to medium frequency range, the diameter of which represents the charge transfer resistance and an inclined line in the low frequency range closely related to the diffusion coefficient of Li^+ inside electrode materials.[45,47-49] Note that the 3D electrode has much low charge transfer resistance (R_{ct}≈40 Ω) at the initial state compared to that of the 2D electrode (R_{ct}≈600 Ω). It is appealing that the charge transfer resistance of the 3D electrode still has no rapid increase after 50 (R_{ct}≈50 Ω) and 150 cycles (R_{ct}≈100 Ω), suggesting its superior electronic conductivity. On the contrary, the diameter of semicircle in high to medium frequency range for the 2D electrode abruptly enlarges just after 50 cycles (R_{ct}>1000 Ω), as present in Figure 4j, implying the notably poor kinetics process for Li^+ and electron transports. To further understand the results from a quantitative viewpoint, the fitting curves and equivalent circuits of EIS of 3D NPC@1D Cu_2O NWNs and 2D PC@Cu_2O MPs electrodes after 50 cycles were

obtained in Figure 4k-l. As can be seen clearly, the fitting curves are well consistent with the EIS of 3D and 2D electrodes after 50 cycles. The equivalent circuits used for fitting are shown in the insets of Figure 4k-l, which consists of corresponding circuit models including the electrolyte resistance R_s, charge transfer resistance R_{ct}, Warburg impedance of Li^+ diffusion in electrode W_o and space charge capacitance at electrode/electrolyte interface CPE. The present fitting results exhibit the 3D electrode have much lower R_s (2.0 Ω) and R_{ct} (46.8 Ω) than those of the 2D electrode (R_s=7.3 Ω, R_{ct}=1025.6 Ω), demonstrating that the unique 3D/1D composite nano-configuration is quite beneficial to rapid Li^+ diffusion, electron transport and electrode/electrolyte wettability.

Figure 5 shows the SEM images of 3D NPC@1D Cu_2O NWNs and 2D PC@Cu_2O MPs electrodes after different charge-discharge cycles, respectively. For the 3D structured electrode, no obvious difference in microstructure (morphology, size and distribution) exists before and after cyclings, as indicated in Figure 5a-b. The SEM images in a higher magnification further display the nearly perface 1D NWNs structure clearly as well as no obvious pulverization and detachment of Cu_2O occur from 3D matrix even after elongated charge-discharge (150) cycles, indicative of its superior structure stability with good binding force between active material and 3D matrix. This is mainly due to the reliable 3D/1D composite nano-configuration with much interspace providing ample room for accommodation of volume variation and the in-situ growth of active material on 3D matrix without additional binders and conductive agents. In clear contrast, the microstructure and surface morphology of 2D

PC@Cu_2O MPs electrode after cyclings were presented in Figure 5c-d. It can be found readily that the large cracks, severe pulverization and exfoliation of active material can be seen just after 10 cycles, as well as the complete collapse and disruption of electrode structure occur after relatively short (50) cycles. This is closely related to the typical size change, large volume expansion and inadequate stress buffering during repeated charge-discharge processes. Note that the present findings are quite different from its original state in Figure S3 (ESI†). Additionally, the stress distributions of the 2D and 3D electrodes after Li^+ insertion reaction can be evaluated further by molecular dynamics (MD) simulation, as displayed in Figure 5e-h. Evidently, the relatively large stress concentration and poor structure integrity can be identified in the 2D electrode after Li^+ insertion, which would be undoubtedly easier to cause the failure of electrode compared to the 3D one (see ESI† for detailed MD analysis, Note 1). Therefore, both the experimental and simulation results clearly demonstrate that the 2D planar configuration cannot buffer the huge volume variation enough during repeated lithiation/delithiation processes (especially at high rates), eventually giving rise to the terrible electrochemical performance.

Compared to the conventional 2D electrode, the unique 3D NPC@1D Cu_2O NWNs electrode, fabricated by one-step UPO assisted dealloying protocol, possesses the extremely superior Li storage performance (ultrahigh specific capacity, good cycling stability and excellent rate capability), which can be ascribed to the following four main aspects. (1) 1D Cu_2O NWNs with large specific areas and good permeability can provide ideal condition for electrolyte diffusion and abundant active sites for lithiation

reaction to achieve the high specific capacity. (2) The reliable 3D/1D composite nano-configuration with much interspace can effectively accommodate the huge volume variation and mechanical strain during repeated charge-discharge processes, resulting in the good cycle stability. (3) The in-situ growth of single-crystal Cu_2O NWs on NPC matrix with good conductivity can markedly enhance the binding force and reduce the charge transfer resistance between active material and current collector to gain the excellent rate capability. (4) The freestanding monolithic structure without additional binders and conductive agents can ensure the excellent structural integrity, prevent the electrode from pulverization and fragmentation, and improve the energy and power densities as it is assembled into cells. Therefore, this work has significant implication for rational design and preparation of promising nanoporous metal/oxide composite anode candidates towards practical application of high-performance LIBs.

Conclusions

In summary, we develop a facile and effecitve UPO assisted dealloying protocol to synthesize the freestanding monolithic 3D NPC@1D Cu_2O NWNs by one-step electrochemical dealloying of as-cast Mn 35 at.% Cu alloy in an oxygen-containing H_2SO_4 solution at the potential of -0.2 V(SCE). With the structure evolution of 3D nanoporous matrix during dealloying, smallish grass-like Cu_2O NWs can be generated on the surface of NPC firstly and then continuously grows up along the radial and axial directions, eventually resulting in the in-situ formation of 3D NPC@1D Cu_2O NWNs. Their formation mechanism can be well established based on morphology and composition evolutions during the dealloying, which includes three typical stages,

sequentially described as “dealloying of (Mn, Cu) accompanying Cu_2O NWs germination”, “growth of Cu_2O NWs accompanying (Mn, Cu) re-dealloying” and “Cu_2O NWNs coarsening”. Compared to other Cu_xO-based electrode materials reported in the literature, the unique nanocomposites as anode for LIBs exhibit the superior Li storage performance, such as ultrahigh specific capacity, good cyclability and excellent rate capability, which can be attributed to accommodating the huge volume variation during repeated cyclings, providing the abundant active sites for lithiation/delithiation reactions, shortening the electron/ion transport paths inside electrode, and constructing the reliable 3D/1D composite nano-configuration without the use of additional binders and conductive agents, indicative of a promising metal oxide based composite anode candicate for next-generation LIBs.

Confict of Interest

The authors declare no competing financial interests.

Acknowledgements

We give thanks to financial support by the National Natural Science Foundation of China (51604177), the State Key Basic Research Program of PRC (2013CB934001), the Research Grants Council of the Hong Kong Special Administrative Region, China (GRF PolyU152174/17E), the Hong Kong Scholars Program (XJ2014045, G-YZ67), the China Postdoctoral Science Foundation (2015M570784), the International S&T Cooperation and Exchange Program of Sichuan Province (2017HH0068), the “1000 Talents Plan” of Sichuan Province, and the Talent Introduction Program of Sichuan University (YJ201410). Additionally, the authors especially thank Dr. Shanling Wang

(Analytical & Testing Center, Sichuan University) for TEM and HRTEM characterization of samples.

References

1 S. H. Lee, G. Jo, W. Park, S. Lee, Y.-S. Kim, B. K. Cho, T. Lee and W. B. Kim, *ACS Nano*, 2010, **4**, 1829-1836.

2 E. J. Boyd and S. A. Brown, *Nanotechnology*, 2009, **20**, 425201.

3 M. A. Hossain, J. R. Jennings, Z. Y. Koh and Q. Wang, *ACS Nano*, 2011, **5**, 3172-3181.

4 H. J. Snaith and C. Ducati, *Nano Lett.*, 2010, **10**, 1259-1265.

5 J. M. Baik, M. Zielke, M. H. Kim, K. L. Turner, A. M. Wodtke and M. Moskovits, *ACS Nano*, 2010, **4**, 3117-3122.

6 Y. Wang, X. Jiang and Y. Xia, *J. Am. Chem. Soc.*, 2003, **125**, 16176-16177.

7 Q. Kuang, C. Lao, Z. L. Wang, Z. Xie and L. Zheng, *J. Am. Chem. Soc.*, 2007, **129**, 6070-6071.

8 A. P. Alivisatos, *Science*, 1996, **271**, 933-937.

9 T. Hyeon, *Chem. Commun.*, 2003, **0**, 927-934.

10 C. Burda, X. B. Chen, R. Narayanan and M. A. El-Sayed, *Chem. Rev.*, 2005, **105**, 1025-1102.

11 M. S. Balogun, H. Yang, Y. Luo, W. T. Qiu, Y. C. Huang, Z. Q. Liu and Y. X. Tong, *Energy Environ. Sci.*, 2018, **11**, 1859-1869.

12 X. Z. Zhu, J. Xu, Y. P. Luo, Q. F. Fu, G. S. Liang, L. J. Luo, Y. J. Chen, C. F. Lin and X. S. Zhao, *J. Mater. Chem. A*, 2019, **7**, 6522-6532.

13 R. J. Li, X. Z. Zhu, Q. F. Fu, G. S. Liang, Y. J. Chen, L. J. Luo, M. Y. Dong, Q. Shao, C. F. Lin, R. B. Wei and Z. H. Guo, *Chem. Commun.*, 2019, **55**, 2493-2496.

14 G. Q. Diao, M. S. Balogun, S. Y. Tong, X. Z. Guo, X. Huang, Y. C. Mao and Y. X. Tong, *J. Mater. Chem. A*, 2018, **6**, 15274-15283.

15 X. M. Lou, R. J. Li, X. Z. Zhu, L. J. Luo, Y. J. Chen, C. F. Lin, H. L. Li and X. S. Zhao, *ACS Appl. Mater. Interfaces*, 2019, **11**, 6089-6096.

16 B. Long, L. Luo, H. Yang, M. S. Balogun, S. Q. Song and Y. X. Tong, *ChemistrySelect*, 2018, **3**, 6965-6971.

17 P. Poizot, S. Laruelle, S. Grugeon, L. Dupont and J. M. Tarascon, *Nature*, 2000, **407**, 496-499.

18 P. Subalakshmi and A. Sivashanmugam, *J. Alloys Compd.*, 2017, **690**, 523-531.

19 Y. H. Xu, G. Q. Jian, M. R. Zachariah and C. S. Wang, *J. Mater. Chem. A*, 2017, **1**, 15486-15490.

20 L. Zhang, B. Yu, P. Z. Ying, L. Wu, S. L. Chen, J. R. Wang, X. Q. Gu, R. Zhou and Z. H. Ni, *Superlattice Microst*., 2015, **84**, 181-191.

21 G. Q. Yuan, J. B. Zhu, F. C. Xie and X. Y. Chang, *J. Nanosci. Nanotechno*., 2010, **10**, 5258-5264.

22 Y. G. Guo, J. S. Hu and L. J. Wan, *Adv. Mater.*, 2008, **20**, 2878-2887.

23 J. Q. Qi, H. Y. Tian, L. T. Li and H. L. Chan, *Nanoscale Res. Lett.*, 2007, **2**, 107-111.

24 Y. Xia, P. Yang, Y. Sun, Y. Wu, B. Mayers, B. Gates, Y. Yin, F. Kim and H. Yan, *Adv. Mater.*, 2003, **15**, 353-389.

25 C. M. Lieber and Z. L. Wang, *MRS Bull.*, 2007, **32**, 99-108.

26 H. W. Liang, S. Liu and S. H. Yu, *Adv. Mater.*, 2010, **22**, 3925-3937.

27 D. Q. Liu, Z. B. Yang, P. Wang, F. Li, D. S. Wang and D. Y. He, *Nanoscale*, 2013, **5**, 1917-1921.

28 X. Dong, W. B. Liu, X. Chen, J. Z. Yan, N. Li, S. Q. Shi, S. C. Zhang and X. S. Yang, *Chem. Eng. J.*, 2018, **350**, 791-798.

29 W. B. Liu, X. Chen, P. Xiang, S. C. Zhang, J. Z. Yan, N. Li and S. Q. Shi, *Nanoscale*, 2019, **11**, 4885-4894.

30 C. Lee, S. D. Seo, D. Kim, S. Park, K. Jin, D. W. Kim and K. Hong, *Nano Res.*, 2013, **6**, 348-355.

31 H. Wu, M. Xu, Y. Wang and G. Zheng, *Nano Res.*, 2013, **6**, 167-173.

32 X. Jiang, B. Tian, J. Xiang, F. Qian, G. Zheng, H. Wang, L. Mai and C. M. Lieber, *Proc Natl Acad Sci USA*, 2011, **108**, 12212-12216.

33 C. Liu, J. Tang, H. M. Chen, B. Liu and P. Yang, *Nano Lett.*, 2013, **13**, 2989-2992.

34 C. Cheng and H. J. Fan, *Nano Today*, 2012, **7**, 327-343.

35 F. S. Ke, L. Huang, B. C. Solomon, G.-Z. Wei, L. J. Xue, B. Zhang, J. T. Li, X. D. Zhou and S. G. Sun, *J. Mater. Chem.*, 2012, **22**, 17511-17517.

36 M. C. Dixon, T. A. Daniel, M. Hieda, D. M. Smilgies, M. H. W. Chan and D. L. Allara, *Langmuir*, 2007, **23**, 2414-2422.

37 J. Erlebacher, M. J. Aziz, A. Karma, N. Dimitrov and K. Sieradzki, *Nature*, 2001,

410, 450-453.

38 L. Y. Chen, J. S. Yu, T. Fujita and M. W. Chen, *Adv. Func. Mater.*, 2009, **19**, 1-6.

39 J. C. Park, J. Kim, H. Kwon and H. Song, *Adv. Mater.*, 2009, **21**, 803-807.

40 L. Hu, Y. M. Huang, F. P. Zhang and Q. W. Chen, *Nanoscale*, 2013, **5**, 4186-4190.

41 R. Sahay, P. S. Kumar, V. Aravindan, J. Sundaramurthy, W. C. Ling, S. G. Mhaisalkar, S. Ramakrishna and S. Madhavi, *J. Phys. Chem. C*, 2012, **116**, 18087-18092.

42 A. Lamberti, M. Destro, S. Bianco, M. Quaglio, A. Chiodoni, C. F. Pirri and C. Gerbaldi, *Electrochim. Acta*, 2012, **86**, 323-329.

43 H. Wu, G. Zheng, N. Liu, T. J. Carney, Y. Yang and Y. Cui, *Nano Lett.*, 2012, **12**, 904-909.

44 W. Q. Chen, W. F. Zhang, L. Chen, L. X. Zeng and M. D. Wei, *J. Alloys Compd.*, 2017, **723**, 172-178.

45 X. Y. Shen, S. Chen, D. B. Mu, B. R. Wu and F. Wu, *J. Power Sources*, 2013, **238**, 173-179.

46 Y. M. Zhang, K. Wang, Z. H. Yang, Y. M. Zhang, H. Y. Gu, W. X. Zhang, E. R. Li and C. Zhou, *Thin Solid Films*, 2016, **608**, 79-87.

47 W. B. Liu, X. Chen, P. Xiang, S. C. Zhang, J. Z. Yan, N. Li, S. Q. Shi, *Nanoscale*, 2019, **11**, 4885-4894.

48 X. Huang, G. Q. Diao, S. Q. Li, M. S. Balogun, N. Li, Y. C. Huang, Z. Q. Liu and Y. X. Tong, *RSC Adv.*, 2018, **8**, 17056-17059.

49 R. J. Li, Y. R. Pu, J. Xu, Q. F. Fu, G. S. Liang, X. Z. Zhu, L. J. Luo, Y. J. Chen and

C. F. Lin, *Ceram. Int.*, https://doi.org/10.1016/j.ceramint.2019.03.127.

Figure Captions:

Figure 1. (a) Schematic illustration showing the preparation flow graph of the freestanding monolithic 3D NPC@1D Cu_2O NWNs. (b-e) SEM images showing the microstructure of the 3D NPC@1D Cu_2O NWNs by electrochemical dealloying of the Mn 35 at.% Cu alloy sheets in the oxygen-containing H_2SO_4 solution at the potential of -0.2 V(SCE) for 60 min. Parts b and c are the plane views; parts d and e are the section views. Inset in part b is the digital photograph of the Mn 35 at.% Cu alloy sheets before and after the electrochemical dealloying. Scale bar: 4 mm. (f and inset) TEM images showing the microstructure of superficial NWNs and single NW in the 3D NPC@1D Cu_2O NWNs. (g) SAED pattern corresponds to the inset in part f. (h) HRTEM image showing the lattice fringes of single NW. Scale bar: 2 nm. EDX spectra showing the typical chemical compositions of (i) superficial NWNs and (j) cross-sectional nanoporous structure in the resultant products.

Figure 2. SEM images showing the microstructure of monolithic 3D NPC@1D Cu_2O NWNs by electrochemical dealloying of the Mn 35 at.% Cu alloy in the 5 wt.% H_2SO_4 solution at the potential of -0.2 V(SCE) for (a) 10 min, (b) 30 min, (c) 60 min, (d) 80 min. Insets show the entire plane-view images at a lower magnification. (e) Chemical composition variation of the Mn 35 at.% Cu alloy during the electrochemical dealloying. (f) Schematic diagrams showing the dealloying evolution process of as-cast Mn 35 at.% Cu alloy sheets in the oxygen-containing H_2SO_4 solution: (A) pre-dealloying, (B-D) during dealloying, (E) post-dealloying. Stage I: "dealloying of (Mn, Cu) accompanying Cu_2O NWs germination". Stage II: "growth

of Cu_2O NWs accompanying (Mn, Cu) re-dealloying". Stage III: "Cu_2O NWNs coarsening".

Figure 3. (a) Tafel polarization curves of as-cast Mn 35 at.% Cu alloy, metals Cu and Mn in the 5 wt.% H_2SO_4 solution at RT. (b) Current density *versus* time profile for electrochemical dealloying of the Mn 35 at.% Cu alloy in the 5 wt.% H_2SO_4 solution at the potential of -0.2 V(SCE). Inset is the localized magnification curve at the dealloying duration ranging from 50 s to 350 s. (c) Corrosion duration dependence curve of open circuit potential for chemical and electrochemical dealloying of the Mn 35 at.% Cu alloy in the 5 wt.% H_2SO_4 solution at RT. (d-f) CVs of the Mn 35 at.% Cu alloy, metals Mn and Cu in the 5 wt.% H_2SO_4 solution in the voltage window of -0.65 ~ -0.3 V(SCE) at a scan rate of 1 mV s^{-1}.

Figure 4. (a,b) Typical galvanostatic charge-discharge curves of 3D NPC@1D Cu_2O NWNs and 2D PC@Cu_2O MPs electrodes between 0.01 and 3.0 V (vs. Li/Li^+) at the current density of 0.1 mA cm^{-1}. (c,d) CVs of 3D NPC@1D Cu_2O NWNs and 2D PC@Cu_2O MPs electrodes between 0.01 and 3.0 V (vs. Li/Li^+) at a scan rate of 0.1 mV s^{-1}. (e) Cycle performance and coulombic efficiency profiles of 3D NPC@1D Cu_2O NWNs and 2D PC@Cu_2O MPs electrodes. (f) Capacity retention of 3D NPC@1D Cu_2O NWNs and 2D PC@Cu_2O MPs electrodes at different current rates. (g,h) Representative charge and discharge voltage profiles of 3D NPC@1D Cu_2O NWNs electrode at various current densities. (i,j) Nyquist plots of 3D NPC@1D Cu_2O NWNs and 2D PC@Cu_2O MPs electrodes before and after 50/150 cycles. Insets in parts i and j show the corresponding high frequency zones at a higher

magnification. (k,l) Nyquist plots and related fitting curves of 3D NPC@1D Cu_2O NWNs and 2D PC@Cu_2O MPs electrodes after 50 cycles. Insets in parts k and l are their corresponding equivalent circuits.

Figure 5. SEM images of (a,b) 3D NPC@1D Cu_2O NWNs electrode after 50 and 150 charge-discharge cycles and (c,d) 2D PC@Cu_2O MPs electrode after 10 and 50 charge-discharge cycles at the current density of 0.1 mA cm^{-2}. The insets show the corresponding high-magnification images. Scale bars in parts a-b and c-d are 500 nm and 5 μm. The original models and normalized von Mises stress distributions after Li^+ insertion of the (e,f) NWNs and (g,h) MPs electrodes by MD simulation. Insets are their corresponding 3D states.

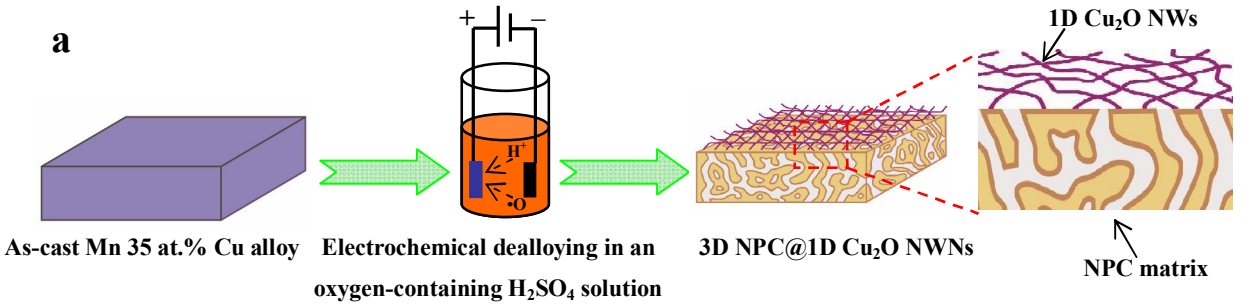
a
1D Cu2O NWs
As-cast Mn 35 at.% Cu alloy
Electrochemical dealloying in an oxygen-containing H2SO4 solution
3D NPC@1D Cu2O NWNs
NPC matrix

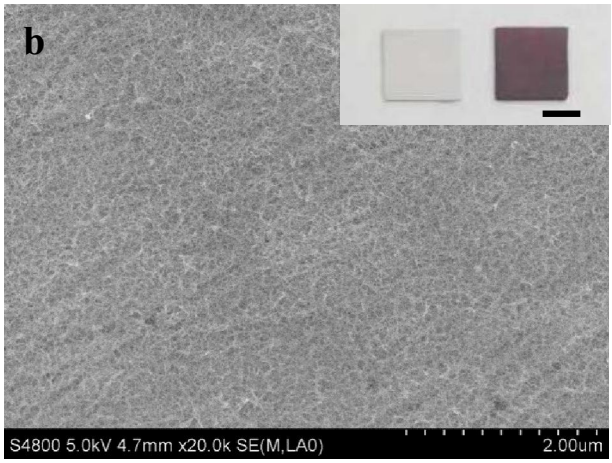
b
S4800 5.0kV 4.7mm x20.0k SE(M,LA0)
2.00um

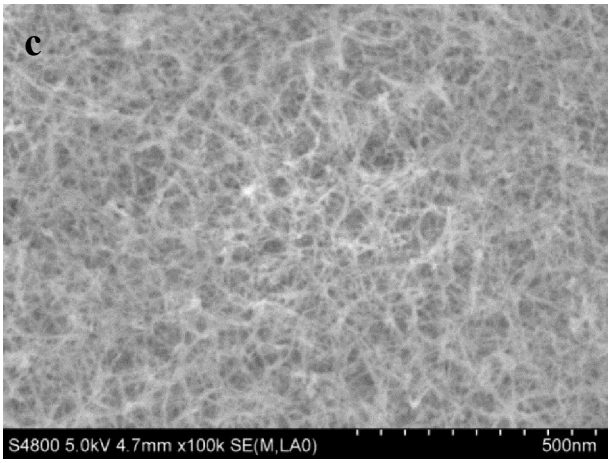
c
S4800 5.0kV 4.7mm x100k SE(M,LA0)
500nm

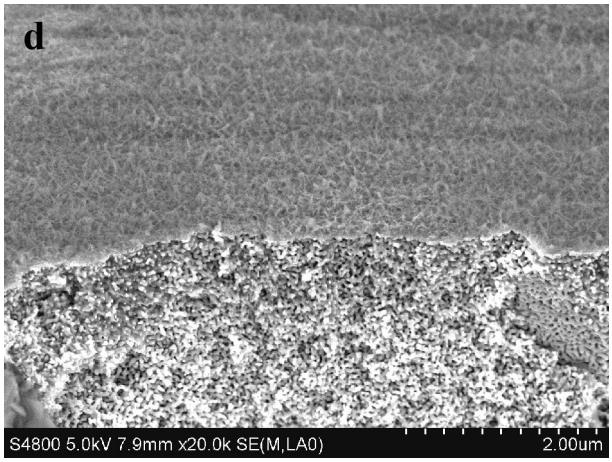
d
S4800 5.0kV 7.9mm x20.0k SE(M,LA0)
2.00um

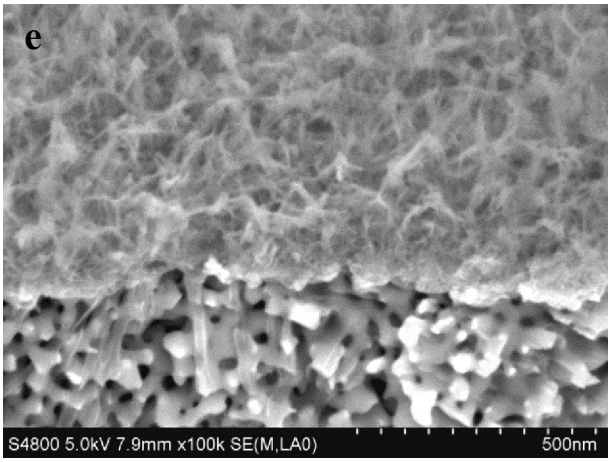
e
S4800 5.0kV 7.9mm x100k SE(M,LA0)
500nm

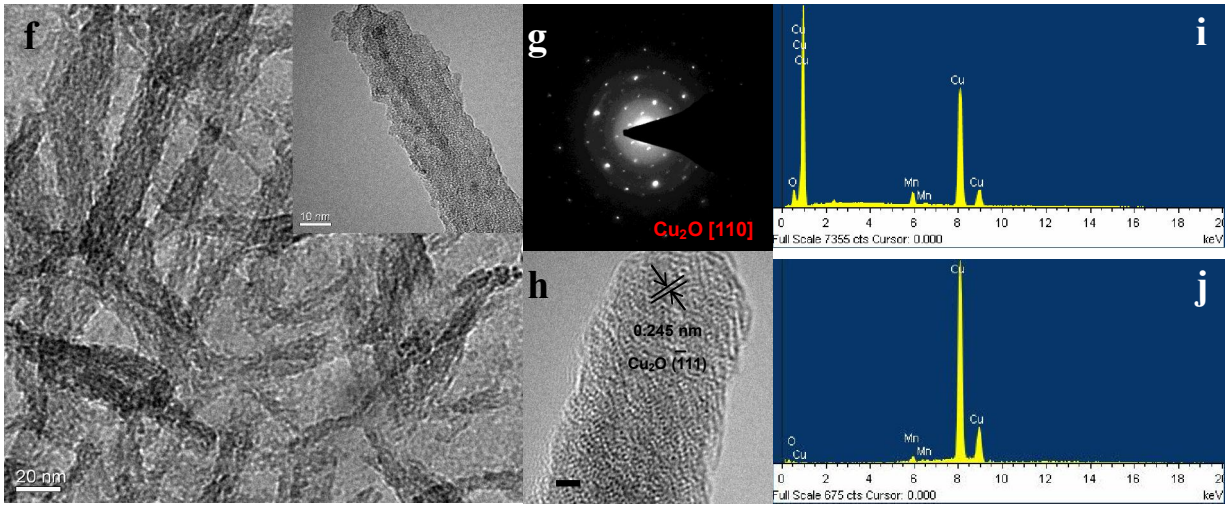
f
20 nm
g
Cu2O [110]
h
0.245 nm
Cu2O (111)
i
Cu
Mn
O
Full Scale 7355 cts Cursor: 0.000
keV
j
Full Scale 675 cts Cursor: 0.000
keV

Figure 1. (a) Schematic illustration showing the preparation flow graph of the freestanding monolithic 3D NPC@1D Cu_2O NWNs. (b-e) SEM images showing the microstructure of the 3D NPC@1D Cu_2O NWNs by electrochemical dealloying of the Mn 35 at.% Cu alloy sheets in the oxygen-containing H_2SO_4 solution at the potential of -0.2 V(SCE) for 60 min. Parts b and c are the plane views; parts d and e are the section views. Inset in part b is the digital photograph of the Mn 35 at.% Cu alloy sheets before and after the electrochemical dealloying. Scale bar: 4 mm. (f and inset) TEM images showing the microstructure of superficial NWNs and single NW in the 3D NPC@1D Cu_2O NWNs. (g) SAED pattern corresponds to the inset in part f. (h) HRTEM image showing the lattice fringes of single NW. Scale bar: 2 nm. EDX spectra showing the typical chemical compositions of (i) superficial NWNs and (j) cross-sectional nanoporous structure in the resultant products.

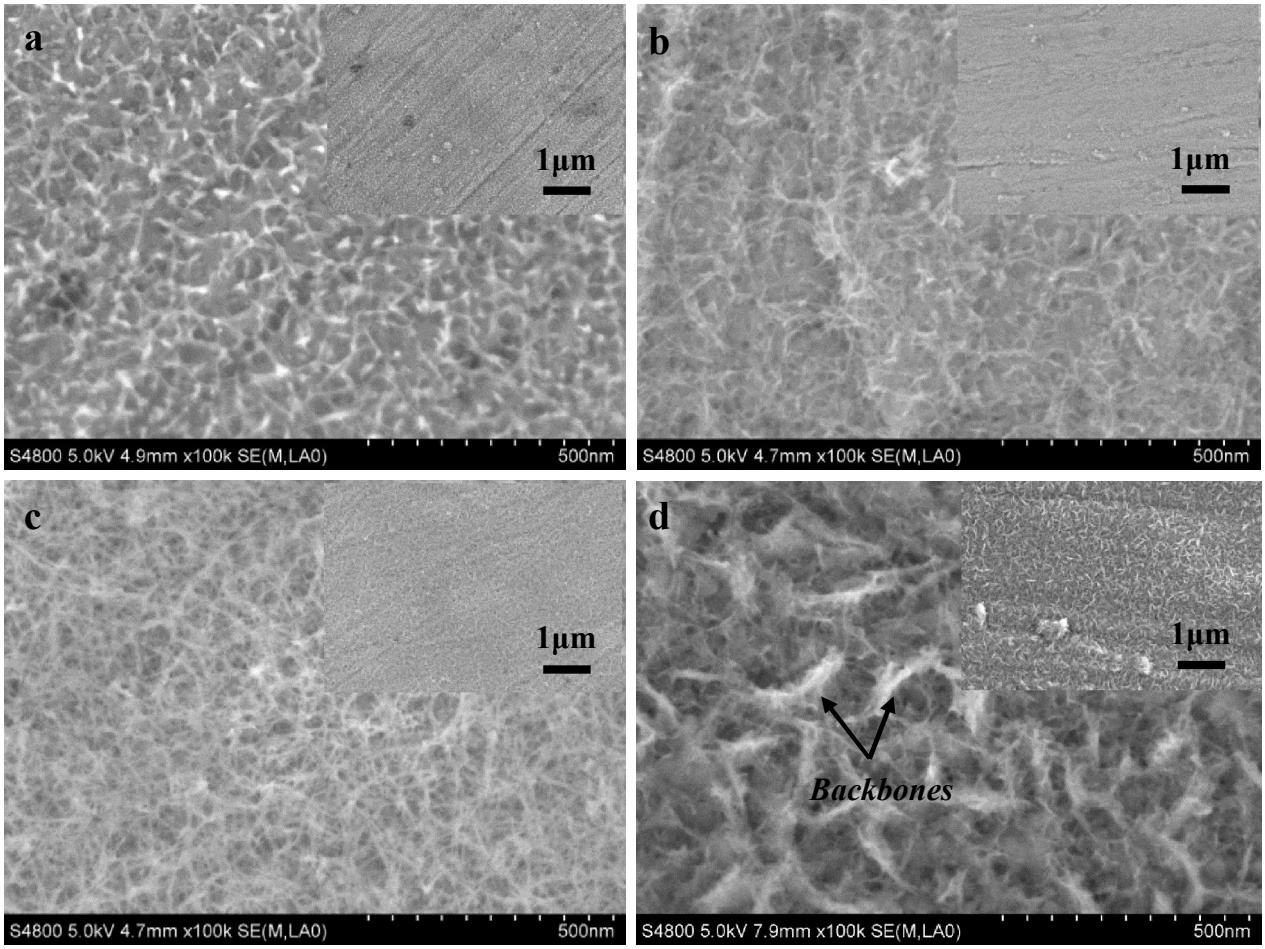
a
1μm
S4800 5.0kV 4.9mm x100k SE(M,LA0)
500nm
b
1μm
S4800 5.0kV 4.7mm x100k SE(M,LA0)
500nm
c
1μm
S4800 5.0kV 4.7mm x100k SE(M,LA0)
500nm
d
1μm
Backbones
S4800 5.0kV 7.9mm x100k SE(M,LA0)
500nm

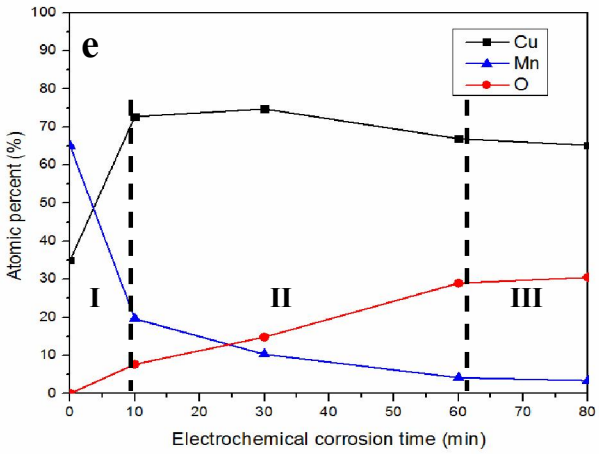
e
Cu
Mn
O
Atomic percent (%)
I
II
III
Electrochemical corrosion time (min)

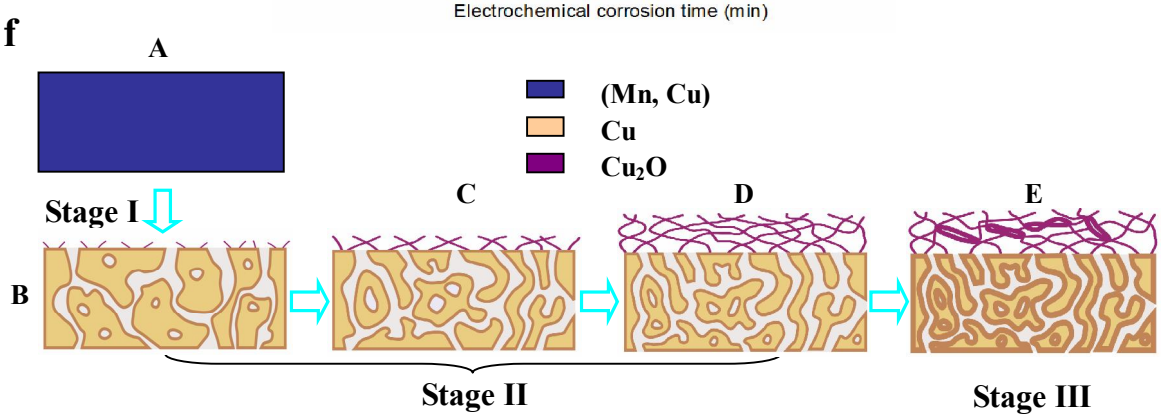
f
A
(Mn, Cu)
Cu
Cu2O
Stage I
B
C
D
E
Stage II
Stage III

Figure 2. SEM images showing the microstructure of monolithic 3D NPC@1D Cu_2O NWNs by electrochemical dealloying of the Mn 35 at.% Cu alloy in the 5 wt.% H_2SO_4 solution at the potential of -0.2 V(SCE) for (a) 10 min, (b) 30 min, (c) 60 min, (d) 80 min. Insets show the entire plane-view images at a lower magnification. (e) Chemical composition variation of the Mn 35 at.% Cu alloy during the electrochemical dealloying. (f) Schematic diagrams showing the dealloying evolution process of as-cast Mn 35 at.% Cu alloy sheets in the oxygen-containing H_2SO_4 solution: (A) pre-dealloying, (B-D) during dealloying, (E) post-dealloying. Stage I: "dealloying of (Mn, Cu) accompanying Cu_2O NWs germination". Stage II: "growth of Cu_2O NWs accompanying (Mn, Cu) re-dealloying". Stage III: "Cu_2O NWNs coarsening".

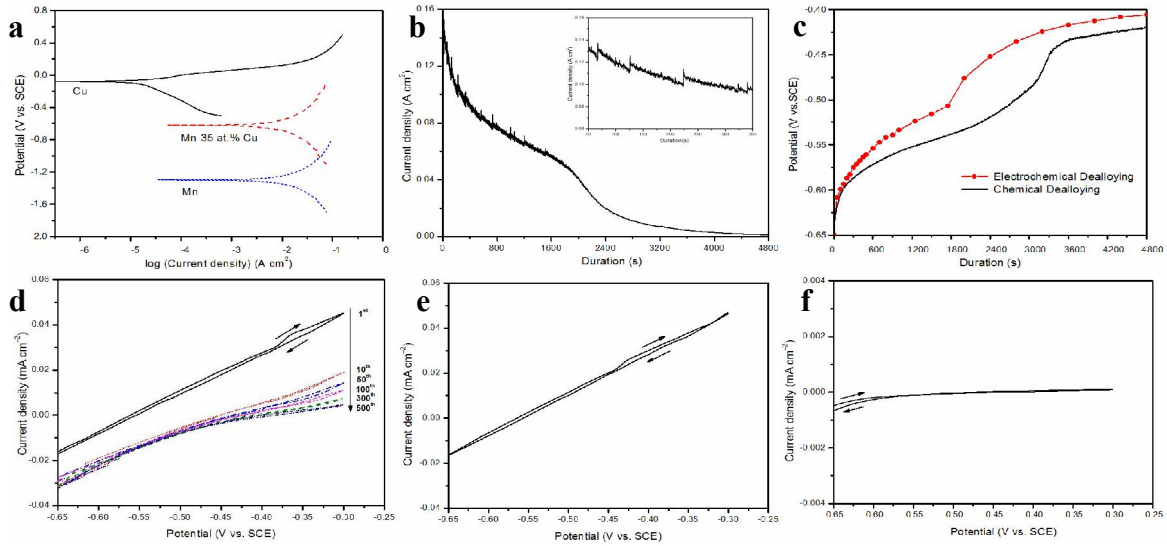

Figure 3. (a) Tafel polarization curves of as-cast Mn 35 at.% Cu alloy, metals Cu and Mn in the 5 wt.% H_2SO_4 solution at RT. (b) Current density *versus* time profile for electrochemical dealloying of the Mn 35 at.% Cu alloy in the 5 wt.% H_2SO_4 solution at the potential of -0.2 V(SCE). Inset is the localized magnification curve at the dealloying duration ranging from 50 s to 350 s. (c) Corrosion duration dependence curve of open circuit potential for chemical and electrochemical dealloying of the Mn 35 at.% Cu alloy in the 5 wt.% H_2SO_4 solution at RT. (d-f) CVs of the Mn 35 at.% Cu alloy, metals Mn and Cu in the 5 wt.% H_2SO_4 solution in the voltage window of -0.65 ~ -0.3 V(SCE) at a scan rate of 1 mV s^{-1}.

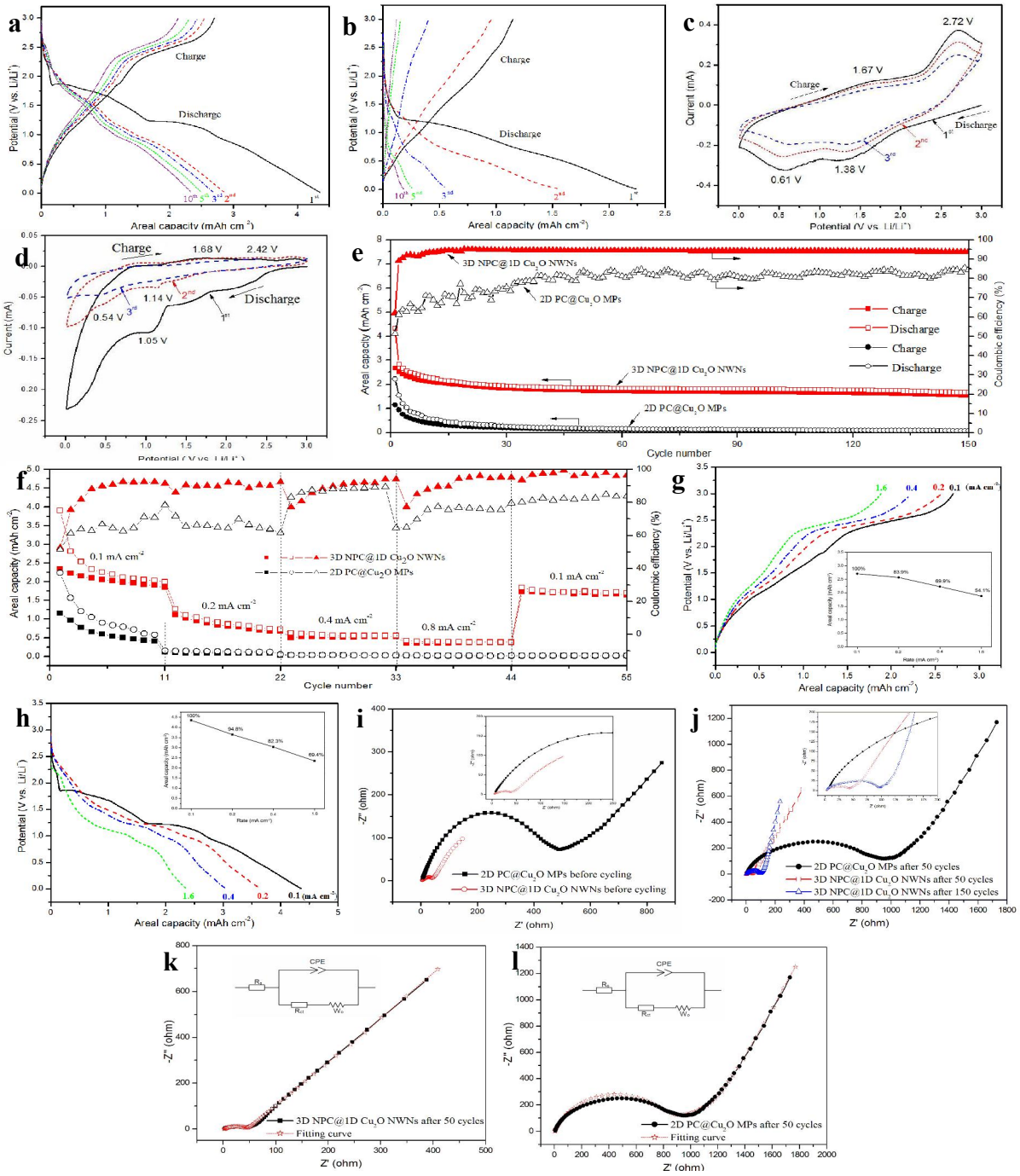

Figure 4. (a,b) Typical galvanostatic charge-discharge curves of 3D NPC@1D Cu_2O NWNs and 2D PC@Cu_2O MPs electrodes between 0.01 and 3.0 V (vs. Li/Li^+) at the current density of 0.1 mA cm^{-1}. (c,d) CVs of 3D NPC@1D Cu_2O NWNs and 2D PC@Cu_2O MPs electrodes between 0.01 and 3.0 V (vs. Li/Li^+) at a scan rate of 0.1 mV s^{-1}. (e) Cycle performance and coulombic efficiency profiles of 3D NPC@1D Cu_2O NWNs and 2D PC@Cu_2O MPs electrodes. (f) Capacity retention of 3D NPC@1D Cu_2O NWNs and 2D PC@Cu_2O MPs electrodes at different current rates. (g,h) Representative charge and discharge voltage profiles of 3D NPC@1D Cu_2O NWNs electrode at various current densities. (i,j) Nyquist plots of 3D NPC@1D

Cu_2O NWNs and 2D PC@Cu_2O MPs electrodes before and after 50/150 cycles. Insets in parts i and j show the corresponding high frequency zones at a higher magnification. (k,l) Nyquist plots and related fitting curves of 3D NPC@1D Cu_2O NWNs and 2D PC@Cu_2O MPs electrodes after 50 cycles. Insets in parts k and l are their corresponding equivalent circuits.

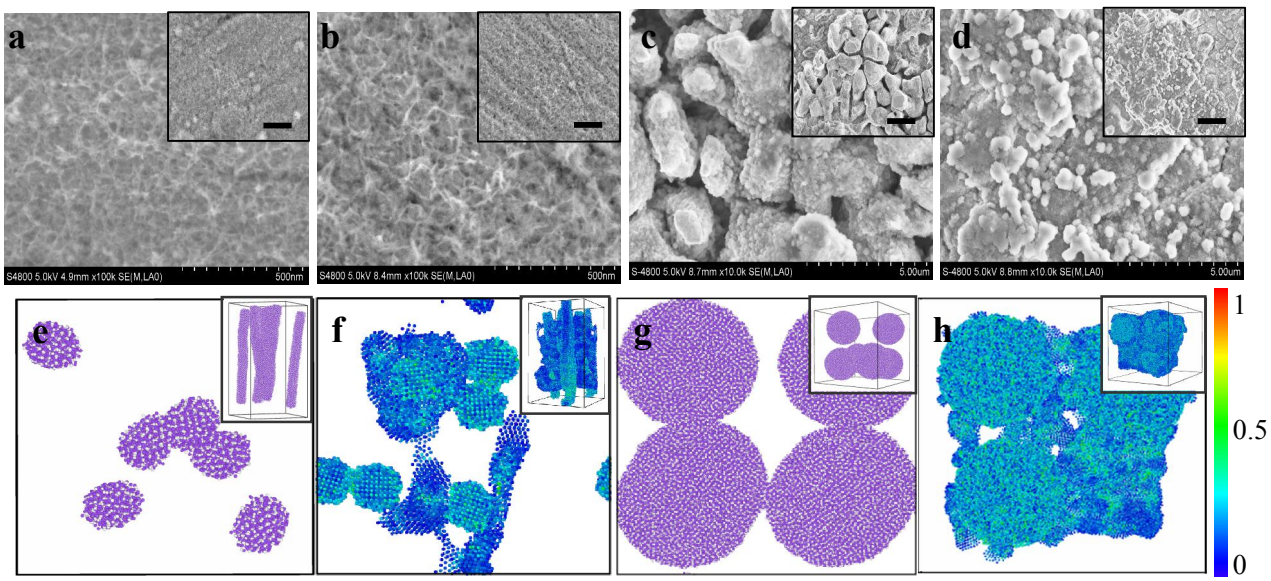

Figure 5. SEM images of (a,b) 3D NPC@1D Cu_2O NWNs electrode after 50 and 150 charge-discharge cycles and (c,d) 2D PC@Cu_2O MPs electrode after 10 and 50 charge-discharge cycles at the current density of 0.1 mA cm^{-2}. The insets show the corresponding high-magnification images. Scale bars in parts a-b and c-d are 500 nm and 5 μm. The original models and normalized von Mises stress distributions after Li^+ insertion of the (e,f) NWNs and (g,h) MPs electrodes by MD simulation. Insets are their corresponding 3D states.